Time-Dependent Nanomechanics of Cartilage

Lin Han,[†] Eliot H. Frank,[‡] Jacqueline J. Greene,[†] Hsu-Yi Lee,[§] Han-Hwa K. Hung,[‡] Alan J. Grodzinsky,[‡§¶‖] and Christine Ortiz[†*]

[†]Department of Materials Science and Engineering, [‡]Center for Biomedical Engineering, [§]Department of Electrical Engineering and Computer Science, [¶]Department of Mechanical Engineering, and [‖]Department of Biological Engineering, Massachusetts Institute of Technology, Cambridge, Massachusetts

ABSTRACT   In this study, atomic force microscopy-based dynamic oscillatory and force-relaxation indentation was employed to quantify the time-dependent nanomechanics of native (untreated) and proteoglycan (PG)-depleted cartilage disks, including indentation modulus E_{ind}, force-relaxation time constant τ, magnitude of dynamic complex modulus $|E^*|$, phase angle δ between force and indentation depth, storage modulus E', and loss modulus E''. At ~2 nm dynamic deformation amplitude, $|E^*|$ increased significantly with frequency from 0.22 ± 0.02 MPa (1 Hz) to 0.77 ± 0.10 MPa (316 Hz), accompanied by an increase in δ (energy dissipation). At this length scale, the energy dissipation mechanisms were deconvoluted: the dynamic frequency dependence was primarily governed by the fluid-flow-induced poroelasticity, whereas the long-time force relaxation reflected flow-independent viscoelasticity. After PG depletion, the change in the frequency response of $|E^*|$ and δ was consistent with an increase in cartilage local hydraulic permeability. Although untreated disks showed only slight dynamic amplitude-dependent behavior, PG-depleted disks showed great amplitude-enhanced energy dissipation, possibly due to additional viscoelastic mechanisms. Hence, in addition to functioning as a primary determinant of cartilage compressive stiffness and hydraulic permeability, the presence of aggrecan minimized the amplitude dependence of $|E^*|$ at nanometer-scale deformation.

INTRODUCTION

Cartilage exhibits time-dependent mechanical behavior that has been documented macroscopically (1–9) and microscopically (10,11) in a variety of loading configurations. These time-dependent properties are essential for proper tissue function, energy dissipation, frequency-dependent stiffening, and reswelling after joint unloading (12). The observed time dependence has been interpreted using continuum theoretical models that include both poroelasticity and viscoelasticity (13–16). The biomechanical behavior of cartilage is related to the tissue's type II collagen network and the negatively charged aggrecan aggregates within the hydrated extracellular matrix (ECM) (12). Viscoelastic relaxation of the solid matrix involves the translational diffusion and reptation of aggrecan aggregate, aggrecan monomers, and glycosaminoglycan (GAG) side chains of aggrecan (17), as well as reconfiguration of the collagen network and associated proteins. Poroelastic energy dissipation is governed by the fluid flow through the porous ECM.

In hydrated cartilage tissue, the collagen fibrils are typically 30–80 nm in diameter, and the gaps between them are on the order of 100 nm (12,18). Between the fibrils, brush-like aggrecan monomers bind to hyaluronan, stabilized by link protein, to form aggregates (19). The aggrecan core protein has a contour length of ~400 nm, and ~40 nm-long GAG chains are substituted onto the core protein ~2–3 nm apart (20). The high density of GAG chains has been identified as the main determinant of the tissue's hydraulic perm-

ability and, thereby, as an important constituent regulating cartilage poroelastic behavior (21). Deformation that takes place at the length scale of these molecules can affect local fixed charge density (22), hydraulic permeability (23), streaming potential (24), and other biophysical mediators of chondrocyte-cell signaling and mechanotransduction (25). The nanomechanics of isolated ECM macromolecules such as type II collagen (26), GAGs (27,28) and aggrecan (29–33) have been studied in vitro. However, there is still a lack of understanding of the ECM mechanical behavior within native tissue subjected to local deformations on the same length scale as macromolecular dimensions.

Hence, the objective of this study was to quantify the time- and frequency-dependent mechanics of native cartilage at deformation length scales comparable to its ECM molecular dimensions and the fluid flow pore sizes, which provides direct molecular-level insights into how these ECM constituents contribute to the tissue-level cartilage behavior. In this study, atomic force microscopy (AFM)-based techniques were employed to carry out sinusoidal dynamic oscillatory indentation of bovine cartilage disks as a function of oscillation frequency f (~1–316 Hz), using previously reported methods (34,35). The results were compared to data obtained on the same cartilage specimens using classical nanoindentation and force-relaxation loading configurations. The contact radius between the AFM probe tips and the cartilage tissue samples (~1 μm) corresponds to the length scale over which fluid-flow-related poroelastic phenomena can occur (i.e., a homogenized microscale region of the ECM). However, the dynamic deformation amplitudes utilized were in the range of ~2–50 nm, a length

scale as small as the GAG-GAG interstitial spacing (12,20,36) that encompasses the range of estimated pore sizes (21) that govern tissue hydraulic permeability, k, and, correspondingly, the degree of poroelastic fluid flow. This length scale also corresponds to the dimensions of the ECM macromolecular components (12,18–20) that contribute to elastic and viscoelastic molecular interactions. The contributions of poro- and viscoelasticity to the observed cartilage time dependence were investigated by relating the results to the associated length- and timescales of these mechanisms. By comparing the dynamic nanomechanical properties of native (untreated) and proteoglycan (PG)-depleted cartilage disks, the observed time and frequency dependence were interpreted in the context of the macromolecular structure and properties of the ECM constituents (e.g., collagen and aggrecan).

METHODS

Sample preparation

Cartilage disks (9 mm in diameter and ~0.5 mm thick) were harvested (37) from the middle zone of femoropatellar groove articular cartilage of 1- to 2-week-old bovine calves and maintained in sterile phosphate-buffered saline (PBS, without Mg^{2+}, Ca^{2+}) with protease inhibitors for <24 h before testing. Additional groups of disks were digested with 1 mg/mL trypsin in 0.15 M NaCl and 0.05 M Na_3PO_4, pH ~7.2 (Sigma-Aldrich, St. Louis, MO), followed by digestion with 0.1 U/mL chondroitinase-ABC in 0.15 M NaCl and 0.05 M Tris-HCl, pH ~8.0 (Seikagaku, Tokyo, Japan), both for 24 h at 37°C. Together, these enzyme treatments resulted in loss of >95% of matrix aggrecan, the most abundant PG in cartilage (38), as assessed by the GAG content via the dimethylmethyleneblue dye binding assay (39). It has been reported that the trypsin digestion does not produce any significant structural change in the collagen fibrillar network, either microscopically (40) or macroscopically (41), or the intrinsic tensile strength of collagen fibrils (42).

AFM-based nanomechanics experiments

Cantilever probe tips

Square pyramidal probe tips were employed with an end radius of $R \sim$ 50 nm, half-open angle of the pyramidal face of $\alpha \sim 35°$, nickel-plated tip D, silicon nitride V-shaped cantilever, and nominal spring constant, k, ~0.58 N/m (Veeco, Santa Barbara, CA), as well as spherical borosilicate colloidal probe tips ($R \sim 2.5$ μm and $k \sim 0.58$ N/m, Bioforce Nanosciences, Ames, IA) (Fig. 1 a). Both probe tips were coated with 2 nm Cr and 50 nm Au, and functionalized with a neutral hydroxyl-terminated self-assembled monolayer (OH-SAM) by immersion in 3 mM 11-mercaptoundecanol ($HS(CH_2)_{11}OH$) (Sigma-Aldrich) ethanol solution for 24 h.

Classical nanoindentation

AFM-based classical nanoindentation were carried out in PBS using a maximum load of ~70 nN in force mode, using a MultiMode AFM with a PicoForce piezo and Nanoscope IV controller (Veeco) over a range of constant z-piezo displacement rates (0.1–10 μm/s), where the closed-looped PicoFoce piezo in the z-direction (perpendicular to the sample plane) enabled the precise control and quantification of indentation force and depth. For each indentation curve, the cantilever deflection (in Volts) and z-piezo displacement (in μm) were converted and averaged to quantify the indentation force-depth data (see Appendix A in the Supporting Material). Three cartilage disk specimens were tested for each treatment condition (i.e., PG-depleted and untreated); separate groups of three disks each were used for testing with spherical and pyramidal probe tips. For each disk specimen, indentation was performed at two to three different locations on relatively flat regions (surface roughness <40 nm for 5 μm × 5 μm scans). At each location, indentation was repeated 10 times at 1 and 10 μm/s z-piezo displacement rate, and five times at 0.1 μm/s, with enough wait time between each repeat.

Force relaxation

Force-relaxation experiments were carried out at the same locations as the classical nanoindentation experiments via a number of programmed sequences as follows. 1), First, the sample was indented using the closed-loop force mode at a constant z-piezo displacement of ~2 μm at 1 μm/s up to a maximum load of ~85 nN, as described above. 2), The system
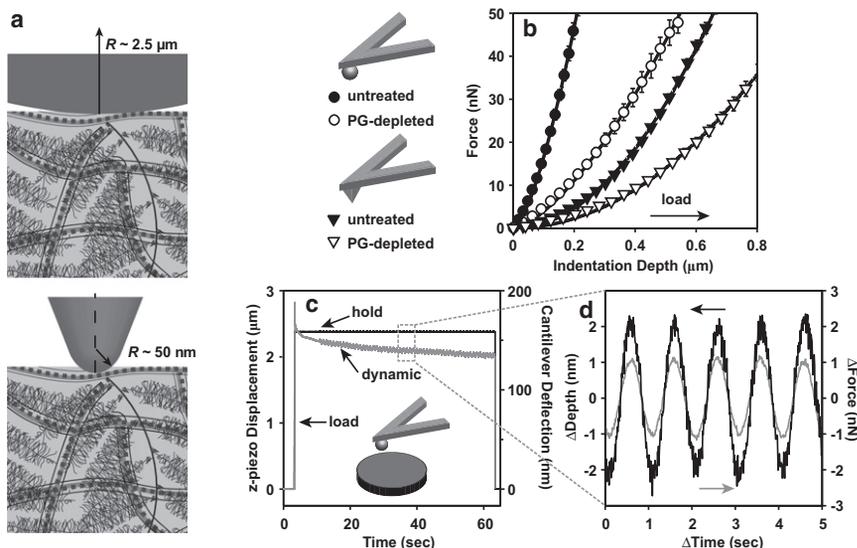

FIGURE 1 (a) Schematic of AFM-based nano-indentation of cartilage and its extracellular matrix components via spherical and pyramidal tips, adapted from Loparic et al. (56). (b) Typical force-indentation depth curves taken from a single location on untreated and PG-depleted cartilage disks using hydroxyl-functionalized spherical ($R \sim 2.5$ μm) and pyramidal ($R \sim 50$ nm, half-open angle of the pyramidal face $\alpha \sim 35°$) probe tips at 10 μm/s z-piezo displacement rate (mean ± SD of 10 repeats at each location to show the repeatability of the indentation at the same location). Data were analyzed using the effective contact point determination algorithm in Appendix A in the Supporting Material, and are shown with corresponding analytical model fits based on Eqs. 1 and 2 (solid lines). The number of data points shown here was reduced to increase clarity. (c) z-Piezo displacement and cantilever deflection data versus time during a typical force-relaxation experiment (~2.3 μm z-piezo displacement applied at 10 μm/s, followed by 60-s hold at constant z-piezo displace-

ment); a sinusoidal z-piezo displacement (1 Hz, ~4 nm amplitude) was then initiated after ~15 s of the holding period, superimposed onto the static displacement. (d) Sinusoidal steady-state dynamic force and indentation depth for five cycles. All the data from c and d correspond to those using an untreated cartilage disk with a hydroxyl-functionalized neutral spherical probe tip ($R \sim 2.5$ μm) in PBS.

was then changed to the open-loop script mode, in which the cantilever probe tip was programmed to move toward and into the surface at the same z-piezo displacement size and rate, which ensured that the maximum indentation force was kept constant at ~85 nN for each test. 3), Immediately after indentation, the piezo was held at a constant position for 60 s before retracting from the specimen, during which period relaxation of indentation force took place. The script mode thus recorded the data for z-piezo displacement and cantilever deflection as a function of time during the indentation and hold period (steps 2 and 3) at a data acquisition rate of 1.02 kHz. At least three repeats were carried out at the same indentation location on each sample, with the time between each repeat sufficient to allow complete recovery.

Dynamic oscillatory loading

After each force-relaxation experiment, a dynamic oscillatory loading experiment was also carried out at the same specimen locations. A function generator (5100, Rockland Scientific, Victoria, British Columbia, Canada) was connected to the PicoForce piezo controller to enable sinusoidal displacement of the z-piezo at specified dynamic oscillation frequencies, f ($f = 1$–316 Hz), and z-piezo displacement amplitudes of ~4, 25, and 125 nm. By subtracting the dynamic oscillation of cantilever deflection (in nm), the dynamic indentation depth amplitudes of cartilage were measured to be ~2, 10, and 50 nm, respectively (see Appendix B in the Supporting Material). Prior to each specified frequency, f, and dynamic z-piezo displacement amplitude, a force-relaxation experiment was first carried out, as described above, and the dynamic oscillation was then superimposed onto the static indentation (Fig. 1 c) during the 60-s hold period at ~15 s after the indentation (step 2 of the force-relaxation experiment). The same z-piezo displacement, cantilever deflection, and time data were acquired at rates of 1.02 kHz for $f < 100$ Hz and 11.74 kHz for $f \geq 100$ Hz (Fig. 1 c). The offset static indentation depths were at 0.43 ± 0.04 μm and 1.01 ± 0.06 μm for the spherical and pyramidal tips on the untreated disks, respectively, and 0.77 ± 0.04 μm and 1.37 ± 0.12 μm (mean $\pm$ SE) for the spherical and pyramidal tips on the PG-depleted disks, respectively. Before the experiments on cartilage, control experiments were performed using a mica sample at the same z-piezo displacement frequencies and amplitudes for system calibration (see Appendix B in the Supporting Material).

Data analysis and modulus calculation

For AFM-based nanoindentation, the tip-sample contact point for each force-depth approach curve was determined via the Golden Section search method (43) (Appendix A in the Supporting Material). The effective indentation modulus, E_{ind}, was computed using analytical contact mechanics models via least-squares linear regression of the experimental loading F-D curves taken at the same sample position and z-piezo displacement rate. For the spherical colloidal probe tip with end radius R on the cartilage sample with thickness $h \gg R$ (here, $h \sim 0.5$ mm, $R \sim 2.5$ μm),

$$F = \frac{4}{3}\frac{E_{ind}}{(1-\nu^2)}R^{1/2}D^{3/2}, \quad (1)$$

where F is the indentation force, D is the indentation depth (Appendix A in the Supporting Material), ν is the Poisson's ratio ($\nu = 0.1$ for both the untreated and PG-depleted bovine cartilage disks (7,44)). For the sharp, pyramidal probe tip (here, $R \sim 50$ nm $<< D$) (45),

$$F = \frac{1.4906}{2}\frac{E_{ind}}{(1-\nu^2)}\tan \alpha D^2, \quad (2)$$

where α is the half-open angle of the pyramidal face ($\alpha = 35°$, as measured with a scanning electron microscope (6060, JEOL, Peabody, MA). The analytical models (Eqs. 1 and 2) were used to account for the indentation geometry. It should be noted that E_{ind} is actually time- and rate-dependent (nonequilibrium), and hence, is utilized to assess trends in cartilage mechanical response to different experimental conditions (e.g., tip geometry and PG depletion) at a given indentation rate.

For each force-relaxation experiment, the loading data were first analyzed as described above to calculate the indentation depth, D. During the subsequent 60-s hold period, the z-piezo position (the sum of the cantilever deflection, d, and indentation depth, D) was held constant. The cantilever deflection decreased over time due to force relaxation, and the indentation depth increased subsequently to a small extent (~5–7%). The time-dependent instantaneous indentation modulus, $E_{ind}(t)$, was calculated via the analytical models (Eqs. 1 and 2) to account for the geometry and the change in both F and, to a much smaller extent, D during the hold period (Fig. 2 b). The equilibrium indentation modulus (after completion of relaxation), $E_{ind,0}$, and the longest relaxation time constant, τ, were computed via a least squares nonlinear regression based on a three-element spring-dashpot model,

$$E_{ind}(t) = E_{ind,0} + E_{ind,1}\exp(-t/\tau). \quad (3)$$

For the nanometer-scale dynamic oscillatory loading experiments, the amplitudes of sinusoidal force, $\tilde{F}$, and indentation depth, $\tilde{D}$, and the phase lag, δ, between them, were calculated at randomly selected intervals starting at ~15 s after the initiation of dynamic z-piezo displacement. During this period, the dynamic oscillatory deformation was observed to be at steady state as $\tilde{F}$, $\tilde{D}$, and δ remained statistically constant over time. The calculation utilized five loading cycles at each frequency (e.g., Fig. 1, c and d; Appendix B in the Supporting Material). Within the dynamic oscillation region of Fig. 1 c, this calculation procedure was repeated 100 times, and the mean values of $\tilde{F}$ and $\tilde{D}$ amplitudes and phase angle δ were obtained. Thus, the total force, F, including static and dynamic components, can be described using the Hertz model with a Taylor series expansion in the indentation depth, D (46),

$$F \approx \frac{4}{3}R^{1/2}\left(\frac{E_{ind,0}}{1-\nu^2}D^{3/2} + \frac{3}{2}\frac{|E^*|}{1-\nu^2}D^{1/2}\tilde{D}\right), \quad (4)$$

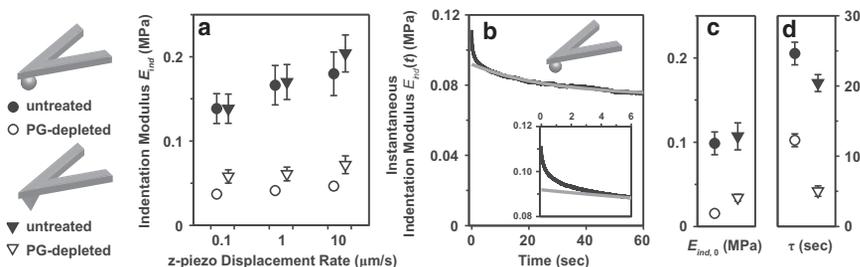FIGURE 2 (a) Indentation modulus, E_{ind}, of untreated and PG-depleted cartilage disks at z-piezo displacement rates of 0.1–10 μm/s, estimated using Eqs. 1 and 2. (b) Instantaneous indentation modulus, $E_{ind}(t)$, directly calculated, using the Hertz model (Eq. 1), from the relaxation data of a single force-relaxation test on an untreated cartilage disk (hydroxyl-functionalized neutral spherical tip, $R \sim 2.5$ μm). The gray line is the best fit of a three-element model (Eq. 3) to the data. (c and d) Equilibrium indentation modulus, $E_{ind,0}$ (c), and characteristic relaxation time constant, τ (d), of untreated and PG-depleted cartilage disks, estimated using Eqs. 1–3. All experiments in a, c, and d were performed using hydroxyl-functionalized spherical and pyramidal probe tips ($n \geq 6$ different locations, mean $\pm$ SE).

where $|E^*|$ is the magnitude of the complex dynamic modulus. Higher-order terms in the expansion were neglected, since the dynamic amplitude, $\tilde{D}$, is at least one to two orders of magnitude smaller than the offset indentation depth, D. Hence, $|E^*|$ was calculated from the oscillatory component,

$$\tilde{F} \approx 2\frac{|E^*|}{(1-\nu^2)} R^{1/2}D^{1/2}\tilde{D}. \tag{5}$$

The same criteria were applied to the data obtained using the pyramidal tip:

$$\tilde{F} \approx 1.4906\frac{|E^*|}{(1-\nu^2)} D\tilde{D}\tan\alpha. \tag{6}$$

We noted that the complex modulus E^* can be represented in terms of its real part (the storage modulus, E') and its imaginary part (the loss modulus, E''):

$$E' = |E^*|\cos\delta, \tag{7}$$

$$E'' = |E^*|\sin\delta. \tag{8}$$

Statistical analysis

To account for multiple measurements at the same indentation locations and to improve the robustness and power of the statistical test, we employed repeated-measures nonparametric statistical tests, which do not assume normal distribution or homoscedasticity of the data (47). Repeated measures analysis of variance (RM-ANOVA) on rank transforms (RT-1) of the entire set of original data and the Friedman test (nonparametric equivalent of one-way RM-ANOVA) were performed on the calculated dynamic modulus $|E^*|$, phase lag δ, storage modulus E', loss modulus E'', and effective indentation modulus E_{ind}. The dynamic deformation frequency, f, amplitude, $\tilde{D}$, and z-piezo displacement rate were taken as within-subject factors, whereas tip geometry and PG depletion were taken as between-subject factors. The Mann-Whitney U test (nonparametric equivalent of Student's t-test) was performed on the equilibrium modulus, $E_{ind,0}$, and relaxation time constant, τ. In all the tests, a p-value of <0.05 was taken as statistically significant. For all statistical tests, data measured from different disks for the same experimental condition (e.g., enzymatic treatment, tip geometry) were pooled, as no significant difference ($p > 0.05$ for E_{ind}, $E_{ind,0}$, τ, $|E^*|$, and δ) was found between the specimens using a two-way RM-ANOVA on RT-1 for $|E^*|$, δ, and E_{ind} (the specimen number was taken as the between-subject factor, frequency f as the within-subject factor), and Mann-Whitney U test for $E_{ind,0}$ and τ.

RESULTS

Classical indentation

In the applied indentation force range (~0–70 nN), both the untreated and PG-depleted cartilage indentation behavior agreed well with the analytical model fits of Eqs. 1 and 2 (Fig. 1 b; $R^2 > 0.98$ for all fits). Upon PG depletion, the cartilage samples exhibited increased compliance compared to the untreated samples with both spherical and pyramidal tips (Fig. 1 b). E_{ind} increased significantly with increasing z-piezo displacement rate (0.1–10 μm/s) for both untreated and PG-depleted disks, using both spherical and pyramidal tips (Fig. 2 a, Friedman test, $p < 0.01$ for all tests). E_{ind} significantly decreased by ~70–80% after PG depletion (Fig. 2 a). A marginally significant tip geometry dependence was observed for the PG-depleted disks, whereas no signif-

icant tip geometry difference for the untreated disks (two-way RM-ANOVA on RT-1, z-piezo displacement rate as the only within-subject factor, $p < 0.001$ for untreated versus PG-depleted disks, $p = 0.0493$ for the tip geometry on PG-depleted disks).

Force relaxation

Fig. 2 b shows a typical individual force-relaxation experiment expressed in terms of the instantaneous indentation modulus, $E_{ind}(t)$, versus time for the untreated cartilage disk, showing a stiffness relaxation from 0.11 MPa to 0.06 MPa during the 60-s hold period. The three-element model (Eq. 3) fit the observed force-relaxation data well for $t > 5$ s after the initiation of relaxation, but not for $t \leq 5$ s (Fig. 2 b, overall $R^2 > 0.95$ for all experimental data). $E_{ind,0}$ for the untreated cartilage was 0.10 ± 0.01 MPa (mean $\pm$ SE, $n \geq 6$ locations) using the spherical tip, and similar results were found using the pyramidal tip (Fig. 2 c, Mann-Whitney U test, $p > 0.05$). For the PG-treated cartilage, $E_{ind,0}$ for the pyramidal tip was marginally greater than that for the spherical tip (Mann-Whitney U test, $p = 0.0411$) (Fig. 2 c). For both probe tips, PG depletion significantly decreased $E_{ind,0}$ by 70–80% (Mann-Whitney U test, $p = 0.0022$ for both tips). In a similar way, tip geometry significantly affected τ for the PG-depleted disk, with ~65% faster relaxation observed using the pyramidal tip, but not for the untreated disk (Fig. 2 d, Mann-Whitney U test, $p < 0.01$ for PG-depleted disks, $p > 0.05$ for untreated disks).

Dynamic oscillatory loading

For the dynamic oscillatory experiments, $|E^*|$, δ, E', and E'' increased nonlinearly with frequency f in the range of 1–316 Hz for both untreated and PG-depleted cartilage disks, using both spherical and pyramidal tips (Fig. 3), and at all tested deformation amplitudes (data not shown, Friedman test, $p < 0.001$ for all cases). PG depletion significantly reduced $|E^*|$, E', and E'', using both spherical and pyramidal tips (two-way RM-ANOVA on RT-1, f as the within-subject factor, $p < 0.05$ for all data sets). At dynamic deformation amplitude $\tilde{D} \sim 2$ nm, $|E^*|$ was found to be linearly dependent on $f^{1/2}$ for both untreated and PG-depleted disks using both probe tips (Fig. 4). $|E^*|$, E' decreased significantly, and E'' increased significantly with increasing dynamic deformation amplitude, $\tilde{D}$, for PG-depleted disks using both probe tips and for untreated disks using the pyramidal tip (two-way RM-ANOVA on RT-1, f and $\tilde{D}$ as within-subject factors, $p < 0.01$), as shown in Fig. 5, a, c, and d. For the untreated disk measured with the spherical tip, the change in $|E^*|$, E', and E'' with amplitude, $\tilde{D}$, was only marginally significant ($p = 0.0442$ for $|E^*|$, $p = 0.0637$ for E', $p = 0.0393$ for E'').

In addition, the relative percentage drop in $|E^*|$, E', and E'' at higher $\tilde{D}$ with respect to the lowest $\tilde{D}$ (~2 nm) was
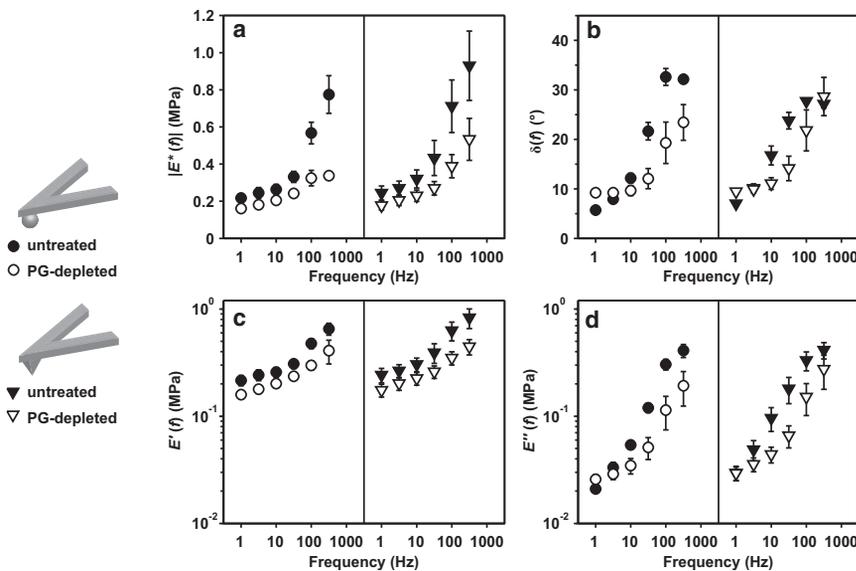
FIGURE 3 Dynamic mechanical properties $|E^*(f)|$ (a), $\delta(f)$ (b), $E'(f)$ (c), and $E''(f)$ (d) versus frequency for untreated and PG-depleted cartilage disks in PBS, using hydroxyl-functionalized spherical ($R \sim 2.5~\mu$m) and pyramidal ($R \sim 50$ nm, $\alpha \sim 35°$) probe tips at ~4 nm z-piezo displacement amplitude (~2 nm cartilage dynamic indentation depth amplitude), estimated using Eqs. 5–8 for $n \geq 6$ different locations (mean $\pm$ SE).

compared for untreated and PG-depleted disks at the tested frequencies (Fig. 5) using two-way RM-ANOVA on the RT-1 of the percentage drops, where f was taken as the within-subject factor, and PG depletion as the between-subject factor. For both spherical and pyramidal tips, PG-depleted disks showed a significantly larger percentage drop in $|E^*|$ and E' (but not E'') at higher D ($p < 0.001$). When D was increased from ~2 nm to ~50 nm, $|E^*|$ of untreated disks decreased by only ~3.4–4.6%, but by ~25–48% for PG-depleted disks.

DISCUSSION

Mechanistic origins of cartilage time-dependent nanomechanics

To assess the mechanistic origins of the observed time- and frequency-dependent dynamic nanomechanical properties, the characteristic poroelastic relaxation frequency, $f_p \sim [(Hk)/L_p^2]$, for the untreated cartilage was estimated to be
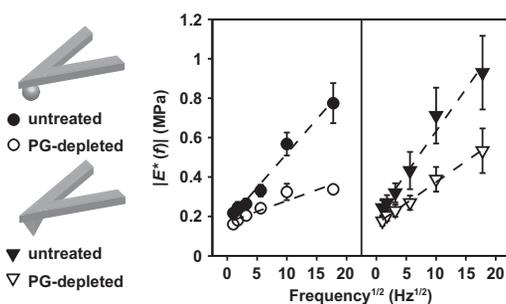

FIGURE 4 Poroelastic-like frequency dependence of $|E^*(f)|$ ($n \geq 6$, mean $\pm$ SE) on $f^{1/2}$ for data obtained using both spherical and pyramidal probe tips, where dashed lines represent least square linear regression between the mean values of $|E^*(f)|$ at each frequency and $f^{1/2}$, $R^2 > 0.88$.

~130 Hz (14). In this calculation, L_p, the characteristic length scale over which fluid flows, was approximated as equivalent to the linear dimension of the tip-sample contact zone: $L_p \sim R \times \arccos(R - D/R) = 1.5~\mu$m for the spherical tip and $L_p \sim D/\cos\alpha = 1.2~\mu$m for the pyramidal tip. H is the equilibrium cartilage modulus, ~0.1 MPa, calculated from the indentation and force-relaxation experiments (Fig. 2, a and c). The hydraulic permeability, k, of 1- to 2-week-old bovine femoropatellar groove cartilage was previously reported to be ~3×10^{-15} m^4 N^{-1}·s^{-1} based on macroscopic (uniaxial confined compression) tests (15). To estimate f_p for the experiments presented here, we first assumed that the same value of k is applicable at microscale dimensions of fluid flow, L_p, since k is dominated in general by GAG-associated pore sizes (21). The resulting f_p is ~130 Hz (for the spherical tip, ~210 Hz for the pyramidal tip), which is the same order as the highest tested frequency values (100–316 Hz) at which the maximum in energy dissipation was observed (Fig. 3 b). $|E^*|$ for the untreated cartilage disks was found to increase linearly with $f^{1/2}$ (Fig. 4), consistent with the expected behavior for poroelastic deformation of cartilage in the frequency range $f < f_p$ (2,15,48), but not for viscoelastic deformation (5,49). In addition, the weak amplitude dependence of $|E^*|$ and δ suggests that poroelasticity also dominates the observed energy dissipation mechanisms even at higher dynamic amplitudes (Fig. 5, a and b), as discussed in more detail below. Intrinsic viscoelastic behavior is expected to be associated with the local rearrangement of aggrecan/GAG and breakage/recombination of aggrecan adhesive interactions (32), and potential reconfiguration of collagen fibrils. Hence, because these possible deformation mechanisms take place at length scales much greater than the dynamic deformation amplitude, $\tilde{D}$ (17), they are expected to make a minimal contribution to the measured frequency dependence at such
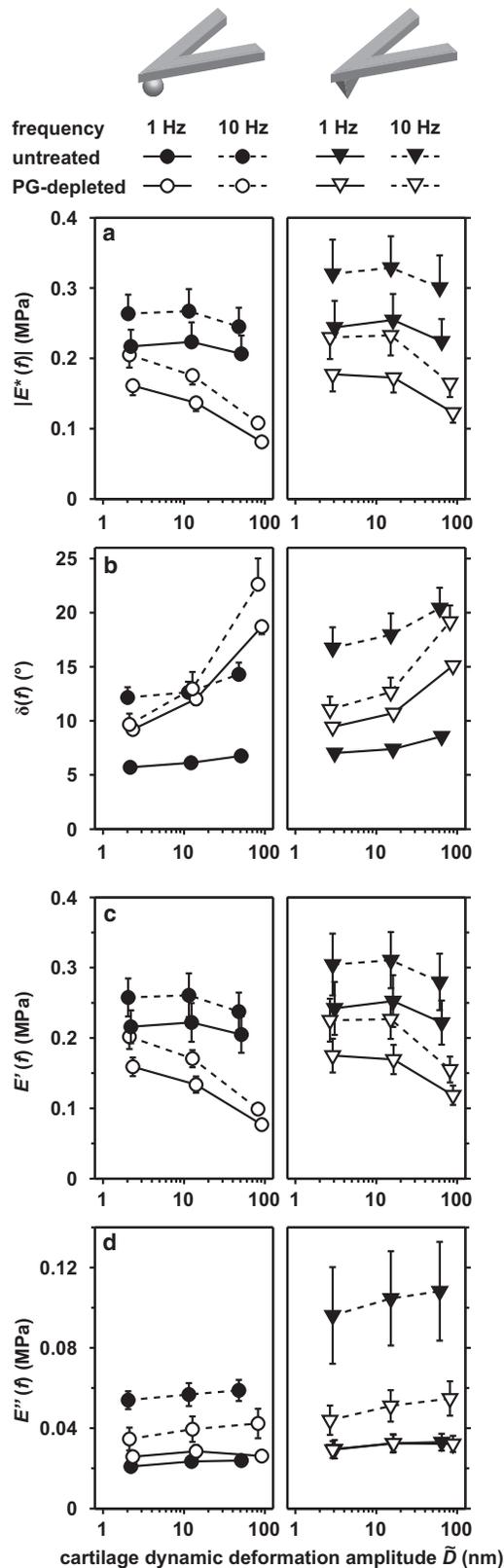
FIGURE 5 Dynamic mechanical properties $|E^*(f)|$ (a), $\delta(f)$ (b), $E'(f)$ (c), and $E''(f)$ (d) as a function of cartilage dynamic deformation amplitude (~2–50 nm) at 1- and 10-Hz deformation frequencies for untreated and PG-depleted cartilage disks in PBS, using hydroxyl-functionalized spher-

small deformation amplitudes. In addition, the known visco-elastic behavior of cartilage disks measured via torsional shear (in the absence of poroelastic behavior) exhibits a maximum of $\delta < 14°$ at larger macroscopic deformation scales (5), which is much smaller than the observed δ of Fig. 3 b at frequencies near f_p. Furthermore, the frequency dependence of $|E^*|$ and δ at higher deformation amplitudes, $\tilde{D}$, remains consistent (Fig. 5), supporting the hypothesis that fluid flow tangential to the direction of dynamic oscillation dominates energy dissipation in this regime, rather than viscoelastic processes, which are most likely dominated by axially directed deformations. Hence, these results suggest that even at fluid-flow length scales much smaller than macroscopic load configurations, and deformation ampli-tudes on the scale of molecular dimensions, fluid-flow-related poroelasticity dominates energy dissipation in the $f = 1$–316 Hz frequency range. It is interesting that recent studies have also revealed that poroelasticity is the dominant mechanism governing the frequency-dependent behavior of newly synthesized cell-associated matrix surrounding indi-vidual chondrocytes, removed from 1- to 4-week alginate culture, and subjected to nanometer-scale dynamic oscilla-tory loading (35).

Since the force-relaxation behavior of untreated cartilage in Fig. 2, b and c, corresponds to $t \gg \tau_p$ (characteristic poroelastic relaxation time, $\tau_p = (1/f_p) \sim 8$ ms) and inden-tation depth ~430 nm, it is hypothesized that the time depen-dence is dominated by the intrinsic viscoelastic behavior of the ECM. The fact that a single relaxation time constant could not fit the relaxation behavior of Fig. 2 b for interme-diate time ($1 < t < 5$ s) suggests the presence of multiple viscoelastic relaxation mechanisms that may be associated with hierarchical structures of cartilage ECM at nano- and microscales (12,17). This viscoelastic behavior could be due to rearrangement of aggrecan/GAGs, adhesive interac-tions between aggrecan (32), reptation of aggrecan mono-mers and aggregates (17), and relaxation of interconnected collagen fibrils. At short times ($t < 1$ s), the force relaxation could be a combined effect of both poro- and viscoelastic mechanisms.

This time-dependent behavior of cartilage was also re-flected in classical nanoindentation tests using the same probe tips. A single indentation test took place over ~0.05 to 10 s, corresponding to z-piezo displacement rates of 10 to 0.1 μm/s, respectively. Hence, based on the above discus-sion, the observed rate dependence of E_{ind} (Fig. 2 a) was likely due to the combined effects of poro- and viscoelas-ticity. The values of E_{ind} are therefore effective responses of cartilage at given indentation rates, resulting from a

ical ($R \sim 2.5$ μm) and pyramidal ($R \sim 50$ nm, $\alpha \sim 35°$) probe tips, estimated using Eqs. 5–8 for $n \geq 6$ different locations (mean ± SE). The amplitude dependence was similar at 100-Hz frequency for both untreated and PG-depleted disks with both probe tips (not shown, for better clarity).

combination of cartilage mechanical properties that affect its time dependence (e.g., $E_{ind,0}$, τ, k). Because both these deformation mechanisms could occur during the indentation test, the contribution of each mechanism could not be individually quantified using only *F-D* indentation curves. Therefore, although classical nanoindentation results did show significant tissue time dependence (Fig. 2 *a*), the dynamic oscillatory indentation combined with force-relaxation tests are advantageous for direct probing of the time- and frequency-dependent behavior of cartilage.

Role of aggrecan in cartilage nanomechanics

Upon aggrecan depletion, ~60–70% reduction in cartilage indentation modulus E_{ind} was observed in both microscale indentation (Fig. 2) and nanoscale dynamic (Figs. 3–5) deformation experiments. These results are consistent with previous tissue level studies showing that aggrecan accounts for >50% of cartilage macroscopic compressive modulus (12,50). Aggrecan is also the major determinant of cartilage tissue permeability, k (12). This is consistent with the increased f_p (~1 kHz) caused by depletion of aggrecan in the dynamic loading experiment (Fig. 3), in which the substantial increase in k outweighs the decrease in H as aggrecan is depleted. In addition, the presence of aggrecan increased the longest relaxation time τ in Fig. 2 *d*, likely associated with the constraints of aggrecan to the relaxation of the collagen network (τ ~ 15 s for the PG-depleted disks versus 25 s for the untreated disks measured via the spherical tip).

Increasing the dynamic amplitude, $\tilde{D}$, from ~2 nm to ~50 nm resulted in a significantly greater decrease in $|E^*|$ for PG-depleted disks compared to untreated disks (Fig. 5). At the higher $\tilde{D}$, which is comparable to collagen fibril diameters and interfibrillar distances (~100 nm), collagen fibrils may undergo increased molecular mobility in the absence of constraints by aggrecan. In a similar way, it is hypothesized that strain softening at the tissue level, observed at large enough deformations, is due to the local release of tension and buckling of the collagen fibrils at deformations that overcome the osmotic swelling pressure of aggrecan (51–53). As buckling would mainly affect elastic deformations, the higher deformation amplitudes, $\tilde{D}$, of Fig. 5 resulted in a significant drop in the elastic storage modulus, E'. At the same time, the increase in E'' and δ at higher $\tilde{D}$ could be related to the viscoelastic energy dissipation due to molecular friction between the buckling collagen fibrils in contact. On the other hand, in the presence of aggrecan, this amplitude-induced viscoelasticity effect was minimized (Fig. 5), as the GAG-GAG electrostatic repulsion can largely reduce the contacts between the ECM macromolecular components (32) and, hence, the viscoelastic energy dissipation associated with macromolecular frictions. As a result, poroelasticity remains the dominating energy dissipation mechanism for the untreated cartilage when increasing the dynamic deformation amplitudes, $\tilde{D}$ (Fig. 5).

Dynamic loading experiments using both spherical and pyramidal probe tips were performed using similar deformation amplitudes and contact areas, and no significant geometry dependence of $|E^*|$ was observed for untreated or PG-depleted disk (Figs. 3–5). In contrast, at larger deformation amplitudes in the indentation force-relaxation experiments, τ and $E_{ind,0}$ exhibited the geometry dependence for PG-depleted but not untreated disks, due to the different stress fields associated with probe tip geometry (Fig. 2, *c* and *d*). Similar to the effect on the dynamic amplitude dependence, in the presence of aggrecan and GAG-GAG electrostatic repulsion, cartilage exhibited more stable and uniform mechanical properties in response to different stress fields.

Comparison to tissue level cartilage dynamic properties

The frequency dependence of cartilage mechanical properties has been probed at the tissue level via dynamic compression in both confined (1,54,55) and unconfined (2,22) compression geometries. The frequency dependence of dynamic modulus and phase angle were well predicted by poroelastic theoretical models (2,15). In this study, fluid flow occurred within cartilage disks mounted between the fluid-impermeable substrate and the fluid-impermeable probe tip in an axisymmetric profile caused by vertical oscillation of the tip. Hence, we compared the observed frequency dependence with that reported for uniaxial unconfined compression of similar bovine calf cartilage disks between fluid-impermeable platens (2). In Fig. 6, the phase lag of the untreated disks measured using the spherical
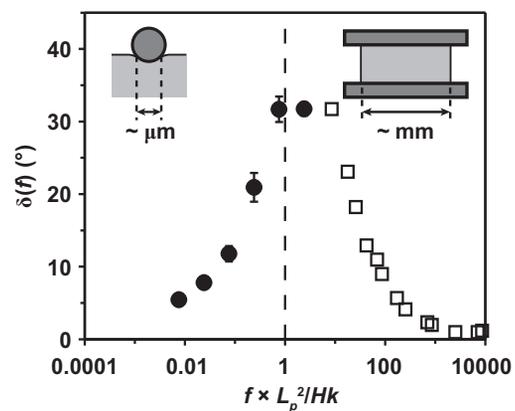

FIGURE 6 Phase angle $\delta(f)$ versus frequency normalized to the characteristic poroelastic relaxation frequency. Data on the left are from nanoscale dynamic oscillatory deformation experiments on normal, untreated bovine calf cartilage specimens, reported here using the spherical tip (R ~ 2.5 μm) at ~2 nm deformation amplitude superposed on a static ~0.43-μm indentation depth (*solid circles*; $n \geq 6$, mean $\pm$ SE). Data on the right are from macroscale unconfined compression experiments on one normal bovine calf cartilage disk, 6.4 mm in diameter and 1 mm thick, using an ~10-μm deformation amplitude superimposed onto an ~200-μm static compression (*open squares*) (adapted from Kim et al. (2)).

probe tip is plotted as a function of frequency normalized by $f_p \sim Hk/L_p^2$, assuming $L_p \sim 1.5\ \mu\text{m}$, $H \sim 0.1$ MPa, and $k \sim 3 \times 10^{-15}\ \text{m}^4\ \text{N}^{-1}\ \text{s}^{-1}$, as discussed previously. Also shown in Fig. 6 is the previously reported phase lag of the dynamic modulus of one cartilage disk, 6.4 mm in diameter and 1 mm thick, tested in uniaxial unconfined compression (2). The macroscopic tests (2) focused on frequencies $f > f_p$, since f_p for the millimeter-sized disks in unconfined compression was ~0.001 Hz (for the given disk geometry), and tests at lower frequencies were not possible. In this study, the frequency range was confined to the region $f \leq f_p$ (~100–300 Hz for the current geometry) due to AFM instrumentation constraints, which prevented measurements at frequencies $> \sim 300$ Hz. Overall, the normalized frequency dependence of the phase lag in Fig. 6 is qualitatively consistent with the poroelastic behavior that would be expected over the complete frequency range ($f_p \in f$) in uniaxial unconfined compression as well as the nanoscale dynamic compression geometry in Fig. 1 a (2). In contrast to poroelasticity, the length scale dependence was much less remarkable for cartilage intrinsic viscoelasticity, as macroscale stress relaxation experiments via unconfined compression (3) resulted in viscoelastic relaxation time constants very similar to those reported by AFM-based nanoindentation (Fig. 2 d).

CONCLUSIONS

In this work, AFM-based indentation methods were used to quantify the time, frequency, and amplitude dependence of untreated and PG-depleted cartilage mechanical properties, including E_{ind} (classical indentation), $E_{ind,0}$, τ (force relaxation), $|E^*|$, E', E'', and δ (dynamic oscillatory loading). An important contribution that emerged from this study involves the comparison between untreated and PG-depleted cartilage disks at the small length scales that yielded insights into the contributions of the ECM molecular components to the measured mechanical properties. In particular, for the dynamic oscillatory experiments on the untreated cartilage disks, it was determined that fluid-flow-induced poroelasticity primarily governs frequency-dependent energy dissipation even at exceedingly small nanometer-scale deformation amplitudes, whereas the longer-timescale force relaxation mainly reflects viscoelasticity. Thus, using contact radii and deformation amplitudes that are several orders smaller than tissue-level testing configurations (2,8), the visco- and poroelastic contributions to cartilage time-dependent mechanical behavior could be deconvoluted. Furthermore, depletion of aggrecan caused a dramatic increase in energy dissipation at higher amplitudes (associated with increased δ and decreased E' in Fig. 5), which is hypothesized to be due to the presence of additional viscoelastic mechanisms, i.e., collagen molecular interactions. Hence, the presence of aggrecan minimizes the amplitude dependence and provides a more uniform and stable mechanical response.

SUPPORTING MATERIAL

Additional text, figures, and references are available at http://www.biophysj.org/biophysj/supplemental/S0006-3495(11)00249-9.

REFERENCES

1. Lee, R. C., E. H. Frank, …, D. K. Roylance. 1981. Oscillatory compressional behavior of articular cartilage and its associated electromechanical properties. *J. Biomech. Eng.* 103:280–292.

2. Kim, Y.-J., L. J. Bonassar, and A. J. Grodzinsky. 1995. The role of cartilage streaming potential, fluid flow and pressure in the stimulation of chondrocyte biosynthesis during dynamic compression. *J. Biomech.* 28:1055–1066.

3. June, R. K., S. Ly, and D. P. Fyhrie. 2009. Cartilage stress-relaxation proceeds slower at higher compressive strains. *Arch. Biochem. Biophys.* 483:75–80.

4. Grodzinsky, A. J., V. Roth, …, V. C. Mow. 1981. The significance of electromechanical and osmotic forces in the nonequilibrium swelling behavior of articular cartilage in tension. *J. Biomech. Eng.* 103:221–231.

5. Hayes, W. C., and A. J. Bodine. 1978. Flow-independent viscoelastic properties of articular cartilage matrix. *J. Biomech.* 11:407–419.

6. Jin, M. S., and A. J. Grodzinsky. 2001. Effect of electrostatic interactions between glycosaminoglycans on the shear stiffness of cartilage: a molecular model and experiments. *Macromolecules.* 34:8330–8339.

7. Buschmann, M. D., Y.-J. Kim, …, A. J. Grodzinsky. 1999. Stimulation of aggrecan synthesis in cartilage explants by cyclic loading is localized to regions of high interstitial fluid flow. *Arch. Biochem. Biophys.* 366:1–7.

8. Kempson, G. E., M. A. R. Freeman, and S. A. V. Swanson. 1971. The determination of a creep modulus for articular cartilage from indentation tests on the human femoral head. *J. Biomech.* 4:239–250.

9. Mow, V. C., M. C. Gibbs, …, K. A. Athanasiou. 1989. Biphasic indentation of articular cartilage—II. A numerical algorithm and an experimental study. *J. Biomech.* 22:853–861.

10. Gupta, S., J. Lin, …, L. Pruitt. 2009. A fiber reinforced poroelastic model of nanoindentation of porcine costal cartilage: a combined experimental and finite element approach. *J. Mech. Behav. Biomed. Mater.* 2:326–337, discussion 337–338.

11. Miller, G. J., and E. F. Morgan. 2010. Use of microindentation to characterize the mechanical properties of articular cartilage: comparison of biphasic material properties across length scales. *Osteoarthritis Cartilage.* 18:1051–1057.

12. Maroudas, A. 1979. Physicochemical properties of articular cartilage. *In* Adult Articular Cartilage. M. A. R. Freeman, editor. Pitman Medical, Tunbridge Wells, UK. 215–290.

13. Biot, M. A. 1956. Theory of propagation of elastic waves in a fluid-saturated porous solid. I. Low-frequency range. *J. Acoust. Soc. Am.* 28:168–178.

14. Mow, V. C., S. C. Kuei, …, C. G. Armstrong. 1980. Biphasic creep and stress relaxation of articular cartilage in compression: theory and experiments. *J. Biomech. Eng.* 102:73–84.

15. Frank, E. H., and A. J. Grodzinsky. 1987. Cartilage electromechanics—II. A continuum model of cartilage electrokinetics and correlation with experiments. *J. Biomech.* 20:629–639.

16. Mak, A. F. 1986. The apparent viscoelastic behavior of articular cartilage—the contributions from the intrinsic matrix viscoelasticity and interstitial fluid flows. *J. Biomech. Eng.* 108:123–130.

17. Papagiannopoulos, A., T. A. Waigh, …, M. Heinrich. 2006. Solution structure and dynamics of cartilage aggrecan. *Biomacromolecules.* 7:2162–2172.

18. Clark, I. C. 1971. Articular cartilage: a review and scanning electron microscopy study. 1. The interterritorial fibrillar architecture. *J. Bone Joint Surg. Br.* 53B:732–749.

19. Hardingham, T. E., and H. Muir. 1972. The specific interaction of hyaluronic acid with cartilage proteoglycans. *Biochim. Biophys. Acta.* 279:401–405.

20. Ng, L., A. J. Grodzinsky, …, C. Ortiz. 2003. Individual cartilage aggrecan macromolecules and their constituent glycosaminoglycans visualized via atomic force microscopy. *J. Struct. Biol.* 143:242–257.

21. Maroudas, A., J. Mizrahi, …, I. Ziv. 1987. Swelling pressure in cartilage. *Adv. Microcirculat.* 13:203–212.

22. Buschmann, M. D., and A. J. Grodzinsky. 1995. A molecular model of proteoglycan-associated electrostatic forces in cartilage mechanics. *J. Biomech. Eng.* 117:179–192.

23. Reynaud, B., and T. M. Quinn. 2006. Anisotropic hydraulic permeability in compressed articular cartilage. *J. Biomech.* 39:131–137.

24. Eisenberg, S. R., and A. J. Grodzinsky. 1988. Electrokinetic micromodel of extracellular matrix and other polyelectrolytes networks. *PhysicoChem. Hydrodyn.* 10:517–539.

25. Guilak, F., A. Ratcliffe, and V. C. Mow. 1995. Chondrocyte deformation and local tissue strain in articular cartilage: a confocal microscopy study. *J. Orthop. Res.* 13:410–421.

26. Sun, Y.-L., Z.-P. Luo, …, K. N. An. 2004. Stretching type II collagen with optical tweezers. *J. Biomech.* 37:1665–1669.

27. Haverkamp, R. G., M. A. Williams, and J. E. Scott. 2005. Stretching single molecules of connective tissue glycans to characterize their shape-maintaining elasticity. *Biomacromolecules.* 6:1816–1818.

28. Seog, J., D. Dean, …, C. Ortiz. 2005. Nanomechanics of opposing glycosaminoglycan macromolecules. *J. Biomech.* 38:1789–1797.

29. Dean, D., L. Han, …, C. Ortiz. 2006. Compressive nanomechanics of opposing aggrecan macromolecules. *J. Biomech.* 39:2555–2565.

30. Han, L., D. Dean, …, A. J. Grodzinsky. 2007. Lateral nanomechanics of cartilage aggrecan macromolecules. *Biophys. J.* 92:1384–1398.

31. Han, L., D. Dean, …, A. J. Grodzinsky. 2007. Nanoscale shear deformation mechanisms of opposing cartilage aggrecan macromolecules. *Biophys. J.* 93:L23–L25.

32. Han, L., D. Dean, …, C. Ortiz. 2008. Cartilage aggrecan can undergo self-adhesion. *Biophys. J.* 95:4862–4870.

33. Harder, A., V. Walhorn, …, D. Anselmetti. 2010. Single-molecule force spectroscopy of cartilage aggrecan self-adhesion. *Biophys. J.* 99:3498–3504.

34. Tyrrell, J. W. G., and P. Attard. 2003. Viscoelastic study using an atomic force microscope modified to operate as a nanorheometer. *Langmuir.* 19:5254–5260.

35. Lee, B., L. Han, …, A. J. Grodzinsky. 2010. Dynamic mechanical properties of the tissue-engineered matrix associated with individual chondrocytes. *J. Biomech.* 43:469–476.

36. Lai, W. M., J. S. Hou, and V. C. Mow. 1991. A triphasic theory for the swelling and deformation behaviors of articular cartilage. *J. Biomech. Eng.* 113:245–258.

37. Sui, Y., J. H. Lee, …, A. J. Grodzinsky. 2009. Mechanical injury potentiates proteoglycan catabolism induced by interleukin-6 with soluble interleukin-6 receptor and tumor necrosis factor α in immature bovine and adult human articular cartilage. *Arthritis Rheum.* 60:2985–2996.

38. Hardingham, T. E., and A. J. Fosang. 1992. Proteoglycans: many forms and many functions. *FASEB J.* 6:861–870.

39. Farndale, R. W., D. J. Buttle, and A. J. Barrett. 1986. Improved quantitation and discrimination of sulphated glycosaminoglycans by use of dimethylmethylene blue. *Biochim. Biophys. Acta.* 883:173–177.

40. Lewis, J. L., and S. L. Johnson. 2001. Collagen architecture and failure processes in bovine patellar cartilage. *J. Anat.* 199:483–492.

41. Bonassar, L. J., E. H. Frank, …, A. J. Grodzinsky. 1995. Changes in cartilage composition and physical properties due to stromelysin degradation. *Arthritis Rheum.* 38:173–183.

42. Schmidt, M. B., V. C. Mow, …, D. R. Eyre. 1990. Effects of proteoglycan extraction on the tensile behavior of articular cartilage. *J. Orthop. Res.* 8:353–363.

43. Lin, D. C., E. K. Dimitriadis, and F. Horkay. 2007. Robust strategies for automated AFM force curve analysis—I. Non-adhesive indentation of soft, inhomogeneous materials. *J. Biomech. Eng.* 129:430–440.

44. Kiviranta, P., J. Rieppo, …, J. S. Jurvelin. 2006. Collagen network primarily controls Poisson's ratio of bovine articular cartilage in compression. *J. Orthop. Res.* 24:690–699.

45. Bilodeau, G. G. 1992. Regular pyramid punch problem. *J. Appl. Mech.* 59:519–523.

46. Mahaffy, R. E., S. Park, …, C. K. Shih. 2004. Quantitative analysis of the viscoelastic properties of thin regions of fibroblasts using atomic force microscopy. *Biophys. J.* 86:1777–1793.

47. Conover, W. J., and R. L. Iman. 1981. Rank transformations as a bridge between parametric and nonparametric statistics. *Am. Stat.* 35:124–129.

48. Soltz, M. A., and G. A. Ateshian. 2000. A conewise linear elasticity mixture model for the analysis of tension-compression nonlinearity in articular cartilage. *J. Biomech. Eng.* 122:576–586.

49. Jin, M., E. H. Frank, …, A. J. Grodzinsky. 2001. Tissue shear deformation stimulates proteoglycan and protein biosynthesis in bovine cartilage explants. *Arch. Biochem. Biophys.* 395:41–48.

50. Williamson, A. K., A. C. Chen, and R. L. Sah. 2001. Compressive properties and function-composition relationships of developing bovine articular cartilage. *J. Orthop. Res.* 19:1113–1121.

51. Lanir, Y. 1987. Biorheology and fluid flux in swelling tissues. II. Analysis of unconfined compressive response of transversely isotropic cartilage disc. *Biorheology.* 24:189–205.

52. Schwartz, M. H., P. H. Leo, and J. L. Lewis. 1994. A microstructural model for the elastic response of articular cartilage. *J. Biomech.* 27:865–873.

53. Bursać, P., C. V. McGrath, …, D. Stamenović. 2000. A microstructural model of elastostatic properties of articular cartilage in confined compression. *J. Biomech. Eng.* 122:347–353.

54. Frank, E. H., and A. J. Grodzinsky. 1987. Cartilage electromechanics—I. Electrokinetic transduction and the effects of electrolyte pH and ionic strength. *J. Biomech.* 20:615–627.

55. Soltz, M. A., and G. A. Ateshian. 2000. Interstitial fluid pressurization during confined compression cyclical loading of articular cartilage. *Ann. Biomed. Eng.* 28:150–159.

56. Loparic, M., D. Wirz, …, M. Stolz. 2010. Micro- and nanomechanical analysis of articular cartilage by indentation-type atomic force microscopy: validation with a gel-microfiber composite. *Biophys. J.* 98:2731–2740.

Time-Dependent Nanomechanics of Cartilage (Supporting Material)

Lin Han,[†] Eliot H. Frank,[‡] Jacqueline J. Greene,[†] Hsu-Yi Lee,[§] Han-Hwa Hung,[‡] Alan J Grodzinsky,[‡§¶‖] and Christine Ortiz[†]*

[†]Department of Materials Science and Engineering, [‡]Center for Biomedical Engineernig, [§]Department of Electrical Engineering and Computer Science, [¶]Department of Mechanical Engineering, and [‖]Department of Biological Engineering, Massachusetts Institute of Technology, Cambridge, Massachusetts

APPENDIX

A. Analysis of AFM-based indentation curves

For each AFM-based indentation experiment, the raw data outputs were the cantilever deflection (d_V, in volts) and z-piezo displacement (z, in nm). To calculate forces, F (nN), calibration of the cantilever deflection sensitivity, d_s (nm/V) was first performed via measurement of cantilever bending on a hard mica surface, and the spring constant k (nN/nm) was measured via thermal vibration (1). Force was then calculated as $F = d_V \times d_s \times k$. For each indentation curve, the z-piezo displacement z was adjusted by subtracting the cantilever deflection d (in nm, $d = d_V \times d_s$), $z' = z - d$. Force data F were slightly offset by subtracting a small value (e.g., 10^{-6} nN) from the measured minimum value to ensure positive definite values along the force curve.

To calculate the indentation depth D, the contact point between the probe tip and cartilage disk must be determined. In all the experiments of this study, no attractive or adhesive interactions were observed between the tip and cartilage. Hence, we adapted a previously reported method (2) to determine the effective tip-sample contact point in the absence of adhesion. In order to remove the spurious portion of the curve that contains no detectable force signals, two positions were searched via the cubic spline fit on the loading curve of log F versus z' in the direction of tip moving towards the sample (2). The first position, z_1, was taken as the last data point at which the first derivative of the fit is negative and second derivative is positive ($d\log F/dz' < 0$ and $d^2\log F/dz'^2 > 0$). The second position, z_2, was taken as the last data point prior to z_1 where $d\log F/dz' > 0$ and $d^2\log F/dz'^2 < 0$, or the first data point along the curve if no data point was detected via the former scenario. The noise level of the force data, n_F, was taken as the 95th percentile of log$F$ for the data between z_1 and z_2. The zero force data point, z_0, was determined as the last data point along the curve where the force signal was below the noise level, log$F < n_F$. After the removal of the spurious data ($z' < z_0$), the remaining portion of the F versus z' curve was converted to force (F) versus indentation depth (D) using $D = z' - z_0$.

For indentation on microtomed cartilage disks, there were sometimes small long range repulsion forces between the cartilage and the neutral probe tip prior to tip-sample contact, possibly due to electrostatic repulsion from the negatively charged aggrecan (3) and/or the presence of microtomed collagen fibrils on the cartilage disk surface. The effective tip-cartilage disk contact point, (D_0, F_0), was determined via the Golden Section search method along the F versus D curve. This effective contact point was taken as the point corresponding to the minimal weighted root mean square error from two least square linear regressions: the linear fit in the noncontant region (LSLR of F versus D, $D < D_0$) and the polynomial fit in the contact region (LSLR of ($F - F_0$) versus ($D - D_0$)^m, $m = 1.5$ for spherical tip and $m = 2$ for pyramidal tip), with errors in the noncontact region weighted half (2). The F versus D curve, which represents indentation of the cartilage disk, was thereby corrected by trimming the noncontact region and offsetting the remaining F-D data by (D_0, F_0).

As negligible irreversible plastic deformation was observed upon repeated indentation at the same location (Fig. 1b), we utilized loading curves to estimate the effective indentation modulus E_{ind} via the analytical models Eqs. (1) and (2) assuming linear, isotropic, and elastic material behavior. The validity of the analytical model for the geometry (e.g., Hertz model for spherical indentation) was tested by comparing the modulus calculated via Hertz model to that calculated via finite element modeling, and < 1% difference was found between these two methods. In the tested indentation depth range, fitting different portions of the loading curve yielded similar E_{ind}, suggesting that the cartilage behaved linearly within the tested range (4). Previous AFM-based nanoindentation studies of bovine knee cartilage utilizing the Hertz model and the loading portion of the curve have reported similar E_{ind} values (5,6). Differences in the magnitude of the reported indentation moduli in other studies were possibly due to different cartilage species (7,8), different experimental parameters (e.g., applied force, indentation rate) and data analysis methods (e.g., the Oliver-Pharr method (9) on the unloading curve) (10-12), and/or different magnitudes of deformation (e.g., deformations up to hundreds of μm via an instrumented nanoindenter) (13-17).

B. Calibration and analysis of dynamic oscillatory indentation data

To correct for any systematic errors in the AFM-based dynamic indentation measurements, calibration was first
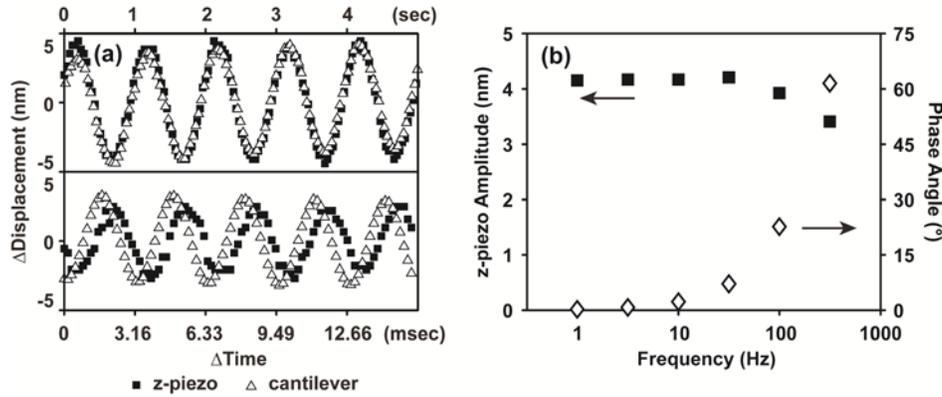
FIGURE A1 (a) Sampling of 5 cycles of z-piezo displacement (solid squares) and simultaneous cantilever deflection data (open triangles) during the dynamic oscillation of z-piezo using a spherical probe tip ($R \sim 2.5$ µm) on a hard mica surface in MilliQ water at 1 Hz, $\sim$ 4 nm amplitude and 316 Hz, $\sim$ 3 nm amplitude. One of every 40 data points were plotted for the 1 Hz (upper panel) and every other data point were plotted for the 316 Hz (lower panel). (b) Estimated z-piezo displacement amplitude (solid squares) and phase angle (deflection – z-piezo displacement, open diamonds) as a function of input frequency f at $\sim$ 4 nm z-piezo displacement amplitudes. All data were obtained on a mica surface in MilliQ water ($n \geq 6$ different locations, mean, SEM was smaller than the size of data symbols).

carried out on a hard mica surface at the same z-piezo displacement frequencies and amplitudes as for the cartilage disks. At each measurement frequency and amplitude, five cycles of the sinusoidal dynamic z-piezo displacement, $\tilde{z}$, and cantilever deflection, $\tilde{d}$, data were randomly chosen in the steady state, which was achieved by 15 seconds after start of the oscillation (Fig. A1a). The z-piezo and deflection data were offset by their means, and subjected to least squares nonlinear regression,

$$\tilde{d}_0 = \tilde{d}_{a0} \sin(2\pi f t + \psi_0), \qquad (A1)$$

$$\tilde{z}_0 = \tilde{z}_{a0} \sin(2\pi f t + \phi_0), \qquad (A2)$$

where $\tilde{d}_0$, $\tilde{z}_0$ and t are the measured dynamic cantilever deflection (nm), z-piezo displacement (nm) and time (sec), f the frequency, while amplitudes $\tilde{d}_{a0}$, $\tilde{z}_{a0}$, and phase angles ψ_0, ϕ_0 are the initial best fit values of those parameters (the subscript "0" denotes the fit from the calibration sample). These initial guesses were set at the maximum of $\tilde{d}_0$ for $\tilde{d}_{a0}$, maximum of $\tilde{z}_0$ for $\tilde{z}_{a0}$, and for ψ_0, ϕ_0, the arcsine value of the first deflection/z-displacement data point normalized by the maximum. If the fit resulted in $R^2 > 0.8$, the outputs of the fit ($\hat{\tilde{z}}_{a0}, \hat{\tilde{d}}_{a0}, \hat{\phi}_0, \hat{\psi}_0$, where "^" denotes the fit output) were accepted as the values for that one sample. To eliminate possible errors from external noise and random data sampling, for each amplitude and frequency, this procedure was repeated until 50 samples were collected. The final data output values were calculated as the average value from the 50 pairs of regression outputs.

Given the essentially infinite stiffness of mica compared to that of the AFM cantilever, the amplitudes of $\tilde{z}_0$ and $\tilde{d}_0$ were observed to be independent of frequency for $f \leq 100$ Hz, and measurements showed that $\hat{\tilde{z}}_{a0} = \hat{\tilde{d}}_{a0}$ (Fig. A1a, upper panel). However, for $f > 100$ Hz, $\hat{\tilde{z}}_{a0} < \hat{\tilde{d}}_{a0}$ was observed, due to the attenuation of the high frequency z-piezo displacement signal by the low pass filter implemented as part of the z-sensor (18) (Fig. A1a, lower panel). Hence, for $f = 316$ Hz, the values of $\hat{\tilde{d}}_{a0}$ were taken to be the z-piezo displacement amplitudes (Fig. A1b). Changes in the phase angle between $\tilde{z}_0$ and $\tilde{d}_0$ $(\hat{\psi}_0 - \hat{\phi}_0)$ were observed at higher frequencies that were also associated with the low-pass filters and displacement sensors (18) and, to a much lesser extent, the hydrodynamic drag effect (19). Such changes in the phase angle from these calibration measurements were subtracted from experimental (cartilage) data, as described below.

For each dynamic oscillatory curve taken on the cartilage disks, the same sampling procedure, as for the calibration data, was repeated, and least-square nonlinear regression was performed on z-piezo and deflection data, $\tilde{z}$ and $\tilde{d}$,

$$\tilde{d} = \tilde{d}_a \sin(2\pi f t + \psi), \qquad (A3)$$

$$\tilde{z} = \tilde{z}_a \sin(2\pi f t + \phi), \qquad (A4)$$

where t, $\tilde{d}$ and $\tilde{z}$ are the experiment outputs, and the initial values for $\tilde{d}_a$, $\tilde{z}_a$, ψ and ϕ were estimated in the same fashion as for the calibration data. Only fits resulting

in $R^2 > 0.9$ for both cantilever deflection and z-piezo data were accepted. The corresponding complex numbers representing the amplitudes and phase of z-piezo and cantilever deflection were calculated after correction in amplitude ($\hat{\tilde{z}}_a = \hat{\tilde{d}}_{a0}$ for $f = 316$ Hz) and phase angle via calibration:

$$\tilde{\mathbf{d}} = \hat{\tilde{d}}_a \left[\cos\left(\hat{\psi} + \hat{\phi}_0 - \hat{\psi}_0\right) + i \sin\left(\hat{\psi} + \hat{\phi}_0 - \hat{\psi}_0\right) \right], \quad (A5)$$

$$\tilde{\mathbf{z}} = \hat{\tilde{z}}_a \left(\cos\hat{\phi} + i \sin\hat{\phi} \right). \quad (A6)$$

The complex amplitudes (magnitude and phase) of dynamic indentation depth, $\tilde{\mathbf{D}}$, and force, $\tilde{\mathbf{F}}$, were calculated as $\tilde{\mathbf{D}} = \tilde{\mathbf{z}} - \tilde{\mathbf{d}}$, and $\tilde{\mathbf{F}} = \tilde{\mathbf{d}} \times k$, respectively. For each dynamic oscillation curve, the phase $\delta(f)$ between $\tilde{\mathbf{D}}$ to $\tilde{\mathbf{F}}$ and the magnitude of complex dynamic modulus $|E^*|$ were calculated as the average of 100 sampling results using the analytical models, Eqs. (5) and (6), as shown in Figs. 3 – 6.

REFERENCES

1. Hutter, J. L. and J. Bechhoefer. 1993. Calibration of atomic-force microscope tips. *Rev. Sci. Instrum.* 64:1868-1873.
2. Lin, D. C., E. K. Dimitriadis and F. Horkay. 2007. Robust strategies for automated AFM force curve analysis - I. Non-adhesive indentation of soft, inhomogeneous materials. *J. Biomech. Eng.* 129:430-440.
3. Dean, D., L. Han, …, C. Ortiz. 2006. Compressive nanomechanics of opposing aggrecan macromolecules. *J. Biomech.* 39:2555-2565.
4. Mahaffy, R. E., C. K. Shih, …, J. Kas. 2000. Scanning probe-based frequency-dependent microrheology of polymer gels and biological cells. *Phys. Rev. Lett.* 85:880-883.
5. Park, S., K. D. Costa, …, K.-S. Hong. 2009. Mechanical properties of bovine articular cartilage under microscale indentation loading from atomic force microscopy. *Proc. Inst. Mech. Eng. [H].* 223:339-347.
6. Park, S., K. D. Costa and G. A. Ateshian. 2004. Microscale frictional response of bovine articular cartilage from atomic force microscopy. *J. Biomech.* 37:1679-1687.
7. Hu, K., P. Radhakrishnan, …, J. J. Mao. 2001. Regional structural and viscoelastic properties of fibrocartilage upon dynamic nanoindentation of the articular condyle. *J. Struct. Biol.* 136:46-52.
8. Radhakrishnan, P., N. T. Lewis and J. J. Mao. 2004. Zone-specific micromechanical properties of the extracellular matrices of growth plate cartilage. *Ann. Biomed. Eng.* 32:284-291.
9. Oliver, W. C. and G. M. Pharr. 1992. An improved technique for determining hardness and elastic modulus using load and displacement sensing indentation experiments. *J. Mater. Res.* 7:1564-1583.
10. Stolz, M., R. Raiteri, …, U. Aebi. 2004. Dynamic elastic modulus of porcine articular cartilage determined at two different levels of tissue organization by indentation-type atomic force microscopy. *Biophys. J.* 86:3269-3283.
11. Stolz, M., R. Gottardi, …, U. Aebi. 2009. Early detection of aging cartilage and osteoarthritis in mice and patient samples using atomic force microscopy. *Nat. Nanotechnol.* 4:186-192.
12. Loparic, M., D. Wirz, …, M. Stolz. 2010. Micro- and nanomechanical analysis of articular cartilage by indentation-type atomic force microscopy: validation with a gel-microfiber composite. *Biophys. J.* 98:2731-2740.
13. Franke, O., K. Durst, …, K. Gelse. 2007. Mechanical properties of hyaline and repair cartilage studied by nanoindentation. *Acta Biomaterialia.* 3:873-881.
14. Li, C., L. Pruitt and K. B. King. 2006. Nanoindentation differentiates tissue-scale functional properties of native articular cartilage. *J. Biomed. Mater. Res. A.* 78A:729-738.
15. Ebenstein, D. M., A. Kuo, …, L. Pruitt. 2004. A nanoindentation technique for functional evaluation of cartilage repair tissue. *J. Mater. Res.* 19:273-281.
16. Gupta, S., J. Lin, …, L. Pruitt. 2009. A fiber reinforced poroelastic model of nanoindentation of porcine costal cartilage: a combined experimental and finite element approach. *J. Mech. Behav. Biomed. Mater.* 2:326-338.
17. Miller, G. J. and E. F. Morgan. 2010. Use of microindentation to characterize the mechanical properties of articular cartilage: comparison of biphasic material properties across length scales. *Osteoarthritis Cartilage.* 18:1051-1057.
18. Asif, S. A. S., K. J. Wahl, …, O. L. Warren. 2001. Quantitative imaging of nanoscale mechanical properties using hybrid nanoindentation and force modulation. *J. Appl. Phys.* 90:1192-1200.
19. Alcaraz, J., L. Buscemi, …, D. Navajas. 2002. Correction of microrheological measurements of soft samtples with atomic force microscopy for the hydrodynamic drag on the cantilever. *Langmuir.* 18:716-721.